This is an open access article published under a Creative Commons Non-Commercial No Derivative Works (CC-BY-NC-ND) Attribution License, which permits copying and redistribution of the article, and creation of adaptations, all for non-commercial purposes.

ACS AUTHORCHOICE

Inorganic Chemistry

pubs.acs.org/IC

Article

Structural Investigations of $MA_{1-x}DMA_xPbI_3$ Mixed-Cation Perovskites

Wouter M. J. Franssen, Cathy M. M. van Heumen, and Arno P. M. Kentgens*

Cite This: *Inorg. Chem.* 2020, 59, 3730–3739

Read Online

ACCESS | Metrics & More | Article Recommendations | Supporting Information

ABSTRACT: Recently, a number of variations to the hybrid perovskite structure have been suggested in order to improve on the properties of methylammonium lead iodide, the archetypical hybrid halide perovskite material. In particular, with respect to the chemical stability of the material, steps should be taken. We performed an in-depth analysis of the structure of $MAPbI_3$ upon incorporation of dimethylammonium (DMA) in order to probe the integrity of the perovskite lattice in relation to changes in the organic cation. This material, with formula $MA_{1-x}DMA_xPbI_3$, adopts a 3D perovskite structure for $0 < x < 0.2$, while a nonperovskite yellow phase is formed for $0.72 < x < 1$. In the perovskite phase, the methylammonium and dimethylammonium ions are distributed randomly throughout the lattice. For $0.05 < x < 0.2$, the phase-transition temperature of the material is lowered when compared to that of pure $MAPbI_3$ ($x = 0$). The material, although disordered, has apparent cubic symmetry at room temperature. This leads to a small increase in the band gap of the material of about 20 meV. Using ^{14}N NMR relaxation experiments, the reorientation times of the MA and DMA cations in $MA_{0.8}DMA_{0.2}PbI_3$ were established to be 1.6 and 2.6 ps, respectively, indicating that both ions are very mobile in this material, on par with the MA ions in $MAPbI_3$. All of the produced $MA_{1-x}DMA_xPbI_3$ materials were richer in DMA than the precursor solution from which they were crystallized, indicating that DMA incorporation is energetically favorable and suggesting a higher thermodynamic stability of these materials when compared to that of pure $MAPbI_3$.

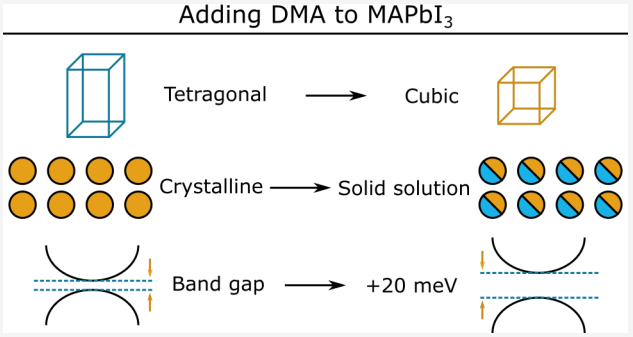

INTRODUCTION

In the past decade, hybrid halide perovskite materials have received considerable attention due to their excellent optoelectronic properties. Starting as light absorbers in dye-sensitized solar cells, perovskite materials are now at the heart of their own class of photovoltaic (PV) devices: perovskite solar cells.[1,2] With a current world record efficiency of 25.2%, perovskite solar cells are in the same league as the best silicon-based devices.[3]

While achieving excellent power conversion efficiencies (PCE), the application of perovskite solar cells is hampered mostly by two major issues: their instability under atmospheric conditions and their high lead content.[4,5] The former issue can be addressed by finding suitable encapsulation techniques or other ways of protecting the active perovskite layer in these devices.[6,7] However, both issues call for addressing the perovskite structure itself: can a perovskite material be developed that is stable, has good optoelectronic properties, and is free of toxic constituents?

To achieve these goals, many variations of the structure of the often-used methylammonium lead iodide ($CH_3NH_3PbI_3$, $MAPbI_3$) have been developed. The concern for stability has led to the addition of other ions, replacing the MA ion fully or partially with cesium, formamidinium (FA), or guanidinium (GUA) to name a few.[8−13] Moreover, iodide can be replaced by bromide.[14,15] The high lead content can be mitigated by the replacement of lead with other divalent cations (e.g., tin) or by a 1:1 mixture of monovalent and trivalent cations (so-called double perovskites).[16] However, to date, these "lead-free" alternatives do not reach the same level of PCE as the lead-containing materials.[17]

The production of these mixed-ion perovskites is most often carried out in either the solution state or the solid state.[18,19] In the solution-state method, the desired components are dissolved in a solvent, which is spin-coated or cooled to produce the perovskite material.[20] In the solid-state method, a selected mixture of solid components is ball-milled to produce the desired mixed-ion perovskite material.[21] The solid-state method has as an advantage that no additives (e.g., the solvent) are necessary, preventing impurities from building into the perovskite material.[22]

Received: November 18, 2019
Published: March 2, 2020

ACS Publications

© 2020 American Chemical Society

https://dx.doi.org/10.1021/acs.inorgchem.9b03380
Inorg. Chem. 2020, 59, 3730–3739

Recently, it has been shown that dimethylammonium (DMA) can be incorporated into $MAPbI_3$, $MAPbBr_3$, and $CsPbI_3$.[23−27] Under both acidic and basic conditions, DMA can be produced by degradation of the dimethylformamide (DMF) solvent and has been identified as an "unknown" constituent of both $MAPbI_3$ and $CsPbI_3$ produced using basic or acidic precursor solutions.[23,25]

Interestingly, the DMA ion has an ionic radius similar to that of formamidinium (FA) and forms similar perovskite-like materials.[28−30] At room temperature, both $FAPbI_3$ and $DMAPbI_3$ are in a yellow phase that is unsuitable for solar cell applications. For $FAPbI_3$, it is known that the addition of MA to the system stabilizes a cubic perovskite phase at room temperature, which for $MAPbI_3$ is stable only above 54 °C and for $FAPbI_3$ is stable only above 185 °C.[31−33] This double perovskite material ($(MA:FA)PbI_3$) has favorable properties and is currently used in most high-performance perovskite solar cells.[14,34] Apart from MA, either Cs or Cs and MA can be used for phase stabilization.[35−37]

From this, it follows that mixed systems of MA and DMA are of interest. Given the similarity between FA and DMA, $MA_{1-x}DMA_xPbI_3$ is expected to occur in compositions (x) which are in the cubic perovskite phase at room temperature. The structural and optical properties of these material are the topics of this article. We used multinuclear solid-state NMR and powder X-ray diffraction for the study of the structure of the $MA_{1-x}DMA_xPbI_3$ system for the full mixing range $0 \leq x \leq 1$. Moreover, the effect of temperature on the structure of these materials was investigated. The optical properties were investigated using reflectance measurements.

EXPERIMENTAL SECTION

Chemicals. Lead iodide (PbI_2) was produced by mixing aqueous solutions of potassium iodide (KI, Merck, 99.5%) and lead acetate ($Pb(CH_3COO)_2{\cdot}3H_2O$, Merck) and was filtered, washed with H_2O, and dried under vacuum at 50 °C. Methylammonium iodide (CH_3NH_3I, MAI) was synthesized by mixing equimolar amounts of hydrogen iodide (Acros, 57 wt % in H_2O) with methylamine (Aldrich, 33 wt % in ethanol), evaporating the solvent at 40 °C, and washing with acetone. Dimethylammonium iodide (DMAI) was made in the same way as MAI but using dimethylamine (Merck, 40 wt % in H_2O). Solvent γ-butyrolactone (GBL) was purchased from Merck (99.0%).

Synthesis. The synthesis of $MA_{1-x}DMA_xPbI_3$ was performed using two methods: via inverse temperature crystallization as described by Saidaminov et al.[38] and via crystallization from concentrated hydroiodic acid as described by Poglitsch and Weber.[20] In both cases, the added amount of methylammonium iodide (CH_3NH_3I, MAI) was partially replaced by dimethylammonium iodide ($(CH_3)_2NH_2I$, DMAI).

For the inverse temperature crystallization, 1.875 mmol (0.864 g) of PbI_2 and 1.875 mmol of MAI were dissolved in 1.5 mL of γ-butyrolacton (GBL) and heated to 60 °C in an oil bath. After the solution was filtered through a PTFE filter, it was heated to 110 °C. After several hours, the resulting crystals were collected from the solution, washed with acetone, and stored under nitrogen. For the syntheses involving DMA, part of the MAI was replaced with the same molar amount of DMAI. MA/DMA ratios, r, of 100:0, 95:5, 90:10, 85:15, and 80:20 were used. For cases with DMA content higher than 80:20, the PbI_2 powder no longer dissolve at 60 °C.

For the synthesis from hydroiodic acid, 1 mmol of lead acetate and 2.5 mmol of MAI/DMAI were dissolved in 2.6 mL of hydroiodic acid and heated to 90 °C in an oil bath. The temperature was slowly lowered to 50 °C over the course of several hours. The resulting crystals were collected from the solution, washed with acetone, and stored under nitrogen. Solutions with MA/DMA ratios of 75:25, 65:35, 55:45, and 0:100 were used.

Solid-State NMR. ssNMR spectra were recorded on a Varian VNMRS system operating in a magnetic field of 20.0 T using a Varian 1.6 mm T3 HXY FastMas probe. Magic-angle spinning (MAS) was performed using boil-off nitrogen. The chemical shift was referenced using adamantane (1.85 ppm) for ^1H, adamantane (low-field line, 38.48 ppm) for ^{13}C, lead nitrate (−3494 ppm) for ^{207}Pb, and ammonium chloride (0 ppm) for ^{14}N, all in the solid state. The spectra were processed using the ssNake software package.[39]

The quantitative ^{13}C spectra were recorded using a single pulse sequence, with a 90° pulse. A recovery delay of 100 s was used. The T_1 values of all of the components were such that this delay can be considered to be quantitative, with the T_1 of $MAPbI_3$ at 9 s and that of $DMAPbI_3$ at 6.8 s (and that of DMA in $MAPbI_3$ at 8 s). These T_1 values were established using a saturation recovery experiment. (See the SI.)

^1H spectra were recorded in an identical way, also using a 100 s delay, with T_1 values of ∼16 s for $MAPbI_3$ and 9.7 s for $DMAPbI_3$. (See the SI.)

The static ^{207}Pb spectra were recorded using a Hahn echo sequence with an interpulse delay of 10 μs and a recovery delay of 5 s (T_1 values are 1.3 s for the 95:5 sample and 1.6 s for $DMAPbI_3$; see the SI). Due to T_2 effects during the sequence, these spectra cannot be considered to be quantitative.

Static ^{14}N spectra were recorded using a solid echo sequence (90−90) with a 150 μs interpulse delay. The recovery time was 4 s (with T_1 values of around 100 ms; see below). Whenever appropriate, multiple spectra recorded with a different spectrometer offset were coadded to achieve a uniform sensitivity across the sometimes broad powder patterns.[40]

Powder XRD. For powder diffraction analysis, crystals were sealed inside a 0.5 mm glass capillary in a glovebox, eliminating air exposure. All diffractograms were recorded using a Panalytical Empyrean diffractometer equipped with a Cu Kα fine-focus sealed tube and a PIXcel3D detector. Data were recorded in capillary mode using Cu $K\alpha_{1,2}$ radiation.

Powder XRD simulations were performed using VESTA.[41] The used CIF structure files were obtained from ICSD and CSD servers, with ICSD no. 239884[42] for $DMAPbI_3$, CSD no. 1509011[43] for cubic $MAPbI_3$, and ICSD no. 241477[44] for tetragonal $MAPbI_3$.

Optical Measurements. The reflectance measurements were performed using a FilMetrics spectrophotometer. The back-reflection (on-axis) of the powder samples was recorded.

Density Functional Theory. Electronic structure and electric field gradient[45] (EFG) calculations were carried out with the Vienna ab initio simulation package (VASP)[46−49] using the projector-augmented wave (PAW) method[50,51] with Becke−Perdew−Ernzerhof (PBE) exchange-correlation functionals[52] and a kinetic energy cutoff of 400 eV. A 2 × 2 × 2 Monkhorst−Pack k-point mesh[53] was used. The nonlocal potential was evaluated in real space.[54] Standard PAW data sets as supplied with the VASP package and recommended in the manual were used[55] (i.e., only the outer-shell s and p electrons were treated as valence), except for Cs and Pb that had frozen $[Kr]4d^{10}$ and [Xe] cores, respectively. Relativistic spin−orbit effects and van der Waals bonding were not accounted for. The ^{14}N quadrupole moment was $Q = 20.44 \times 10^{-31}$ m^2.[56]

We used a 2 × 2 × 2 supercell containing one DMA^+ or MA^+ ion and seven Cs^+ ions, in a manner equivalent to that in our previous work.[57] In this case, a cubic lattice was used, with a lattice constant of 12.63 Å that was established for the 85:15 sample using XRD (vide infra). For this study, we relaxed only the DMA^+/MA^+ coordinates and the coordinates of the iodide ions.

RESULTS

Using the two synthesis methods, materials were produced with different MA/DMA ratios in solution. For the inverse crystallization method (method 1), powders were synthesized from solutions with MA/DMA ratios, r, of 100:0, 95:5, 90:10, 85:15, and 80:20. Using method 2 (crystallization from HI), r values of 75:25, 65:35, 55:45, and 0:100 were used. The

https://dx.doi.org/10.1021/acs.inorgchem.9b03380
Inorg. Chem. 2020, 59, 3730−3739

resulting materials were crushed to fine powders and analyzed using solid-state NMR, powder XRD, and optical reflection. The 100:0 sample was identified as $MAPbI_3$, and the 0:100 sample was identified as $DMAPbI_3$. $MAPbI_3$ consists of corner-sharing PbI_6 octahedra, with the MA cation occupying the cavities between these moieties. At room temperature, the material has a tetragonal crystal structure. $DMAPbI_3$ consists of face-sharing PbI_6 octahedra, forming columns along the c axis. In between these columns reside the DMA cations. The material has a hexagonal crystal structure at room temperature.[42] An illustration of both crystal structures can be found in the SI.

First, we examine the ^{1}H ssNMR spectra of the series of samples in order to investigate and quantify the MA and DMA contents of the produced materials. For $MAPbI_3$ (i.e., for $x = 0$ in $MA_{1-x}DMA_xPbI_3$), the ^{1}H spectrum in Figure 1 shows two

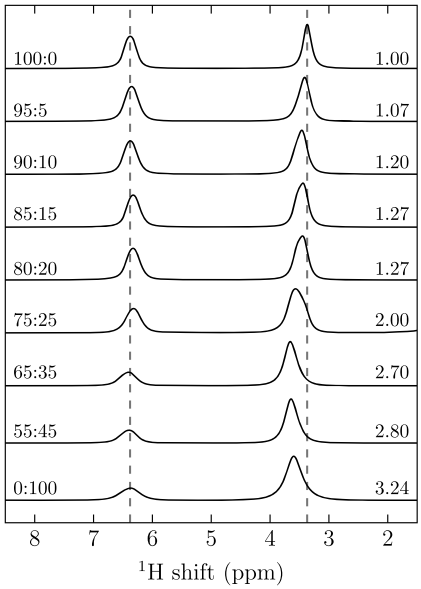

Figure 1. ^{1}H MAS NMR spectra of $MA_{1-x}DMA_xPbI_3$ at 850 MHz using 20−30 kHz MAS. The values on the left are MA/DMA ratios, r, of the solutions used during synthesis. The values on the right represent the NH/CH integral ratio. Dashed lines are visual aides and are at the position of the NH_3 and CH_3 resonances of $MAPbI_3$.

well-separated resonances: one for the CH_3 group (3.4 ppm) and one for the NH_3 group (6.4 ppm).[58] Any DMA ions, if present, lead to two additional resonances at roughly the same position, as was demonstrated in our previous work.[23] These resonances, however, will have a different integral ratio: there are now two CH_3 groups and an NH_2 group, resulting in a 6:2 intensity ratio as opposed to the 3:3 ratio for the MA ions.

Examining the ^{1}H spectra in Figure 1 in cases where DMA was added to the precursor solution, there are some changes with respect to the spectrum of pure $MAPbI_3$ (i.e., the 100:0 case). First, gradually the relative integral of the CH_3 resonance increases when compared to the $NH_{2,3}$ resonance (see the numbers on the right-hand side in Figure 1). Second, changes in peak shape and position occur. At an r value of 75:25, the CH_3 resonance consists of two overlapping line shapes. At 65:35 and with more DMA content, the $NH_{2,3}$ protons resonate at a slightly higher chemical shift. These results suggest that there is an incorporation of DMA in the solid-state material if DMA is added to the precursor solution, in line with earlier observations.[23] High DMA concentrations also lead to a higher NH/CH integral ratio, suggesting that indeed more DMA is incorporated in these cases. The abrupt shift of the NH line for the 65:35 sample and higher DMA contents suggests that a significant structural change occurs at these DMA concentrations.

Quantification of the relative amount of MA and DMA incorporated into these structures is more accurately done using ^{13}C NMR because the wide chemical shift range allows for a better separation of the MA and DMA signals. Both MA and DMA give only a single resonance in the ^{13}C NMR spectrum because the two methyl groups of DMA are identical. The MA signal resonates at ∼30 ppm, and the DMA signal resonates at ∼44 ppm.[23,58] The ^{13}C spectra for the samples are plotted in Figure 2. It is clear that the addition of DMA during

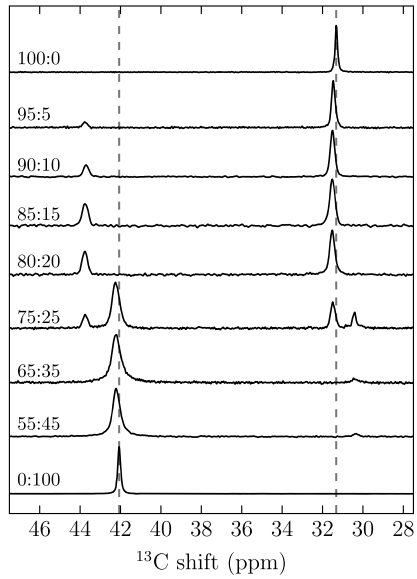

Figure 2. ^{13}C SPE MAS NMR spectra of $MA_{1-x}DMA_xPbI_3$ at 850 MHz using 20−30 kHz MAS and 80 kHz ^{1}H decoupling. The values on the left are MA/DMA ratios of the solutions as used during synthesis. Dashed lines are visual aides and are at the position of the resonance of $MAPbI_3$ (∼31 ppm) and $DMAPbI_3$ (∼42 ppm).

the synthesis leads to an extra resonance at ∼43.5 ppm. The intensity of this DMA resonance increases with increasing DMA content of the solution, indicating that more DMA is incorporated into the $MAPbI_3$ structure at these higher DMA contents in the solution. At an r value of 75:25, a change occurs and four resonances are observed. This is due to the cocrystallization of two separate phases: one is black (like $MAPbI_3$), and the other is yellow (like $DMAPbI_3$). The occurrence of four resonances must be due to the fact that these materials have both MA and DMA incorporated into their structures. This gives MA and DMA ^{13}C resonances for the black, $MAPbI_3$-like material (∼31.5 and ∼44 ppm) as well as (slightly shifted) MA and DMA resonances for the yellow $DMAPbI_3$-like material (∼30.5 and ∼42 ppm). The ^{13}C NMR shifts for these cases are different enough to be identified in the ^{13}C NMR spectra. For DMA contents higher than 35% (65:35), only the yellow, $DMAPbI_3$-like phase is produced, and two resonances are again observed. The change in structure for DMA contents of 35% (65:35) and higher also explains the ^{1}H spectra as described above.

https://dx.doi.org/10.1021/acs.inorgchem.9b03380
Inorg. Chem. 2020, 59, 3730−3739

The pairs of resonances observed in Figure 2 cannot be due to MA or DMA ions in other environments because none of the other likely MA- and DMA-containing materials show ^{13}C resonances at these positions.[23] The materials analyzed here are therefore $MAPbI_3$ with DMA ions incorporated into the lattice and $DMAPbI_3$ with MA ions incorporated into the lattice, which have not been described before. As the spectra in Figure 2 were recorded in a quantitative way, using SPE with an adequately long relaxation delay, the actual MA and DMA contents of all of these materials can now be established from the relative integrated intensities of the lines. Moreover, the basic crystal structure can be derived from these spectra: either $MAPbI_3$ with DMA incorporation or $DMAPbI_3$ with MA incorporation. The results of this analysis are summarized in Table 1. These data show that the $MAPbI_3$ structure is retained

Table 1. MA/DMA Ratio of the Precursor Solution (r) and the Composition (x) of Resulting Solid-State Material $MA_{1-x}DMA_xPbI_3$ for Both the Inverse Crystallization (Method 1) and Crystallization from HI (Method 2)[a]

method	r [MA/DMA]	x	lattice
1	95:5	0.067 ± 0.003	$MAPbI_3$
1	90:10	0.153 ± 0.004	$MAPbI_3$
1	85:15	0.207 ± 0.005	$MAPbI_3$
1	80:20	0.207 ± 0.004	$MAPbI_3$
2	75:25	0.199 ± 0.008/0.723 ± 0.004	mixed
2	65:35	0.896 ± 0.003	$DMAPbI_3$
2	55:45	0.940 ± 0.002	$DMAPbI_3$

[a]Also shown is the main lattice structure of the material.

for values of $x < 0.207$, while the $DMAPbI_3$ structure is obtained for $x > 0.723$. This demonstrates the flexibility of these structures for changes in the content of different organic cations. It seems that structures with $0.207 < x < 0.723$ cannot be formed, suggesting that the $MAPbI_3$ lattice cannot accommodate such a high concentration of DMA ions and equivalently the $DMAPbI_3$ lattice cannot accommodate a high concentrations of MA.

A remarkable effect that follows from the analysis (Table 1) is that the DMA/MA ratio of the produced solid-state materials (i.e., the x value) is always higher than in the precursor solution. This difference in solution and solid-state content has been observed before, in $MAPb(Cl/Br/I)_3$ and $(Cs/FA/MA)PbI_3$.[59,60] The discrepancy in DMA content between the solid and the solution is possible because the yield of the crystallization process is quite low (~10%), meaning that a higher incorporation in the solid state does not deplete the solution of DMA and r can be assumed to be constant during the crystallization process. The higher incorporation of DMA in the solid state suggests that this incorporation is energetically favorable. As the stability of $MAPbI_3$ versus MAI and PbI_2 has been debated, the tendency to form these MA- and DMA-containing perovskite materials can be regarded as an indication of the increased stability of these materials in terms of decomposition to MAI/DMAI and PbI_2.[61,62] This is in line with the results of Nagabhushana et al., who suggest that an increase in the Goldschmidt tolerance factor (in this case, an increase in the size of the organic cation by the partial substitution of MA by DMA) leads to a more stable perovskite structure.[63] A similar effect is observed for the perovskite material where MA and formamidinium (FA) are mixed.[64]

The energy landscape of mixed A-cation perovskites is governed by entropic effects, as has been described by Yi et al.[32] They discuss a system with a mixture of cesium and formamidinium (i.e., $Cs_xFA_{1-x}PbI_3$). For this material, $x \approx 0.5$ is demonstrated to be the lowest-energy form because the entropic effects are maximized at this value. Changes in internal energy (enthalpy) are demonstrated to play only a minor role in the perovskite structure in this case. In our case, the entropic contribution can be considered to follow a similar path and should have $x \approx 0.5$ as an optimum. However, our observations show that $MA_{0.5}DMA_{0.5}PbI_3$ is not formed. Clearly, the entropic advantages of such a system are not enough to overcome the changes in internal energy that must occur. Instead, a material with $x > 0.723$ is formed when the DMA/MA ratio of the precursor solution is increased to above 75:25. This material has a nonperovskite crystal structure and is similar to that of $DMAPbI_3$. Clearly, the perovskite lattice must undergo considerable energetically unfavorable changes to accommodate increasing amounts of the large DMA cation. Forming an $x > 0.723$ material with a different crystal structure is more favorable if the DMA content exceeds a certain threshold.

Apart from the relative MA and DMA contents of the $MAPbI_3$ and $DMAPbI_3$ lattices, the distribution of these ions over the lattice sites is relevant for a proper description of the structure of the material. MA and DMA can be distributed randomly over the material (i.e., as a solid solution) or might cluster in MA- or DMA-enriched regions. In the case of clustering or specific ordering, different regions might possess different properties, which can have a strong influence on the overall material properties. Moreover, it is conceivable that the way MA and DMA are distributed in the material is influenced by the value of x.

One way to study the distribution of the MA and DMA ions throughout the structure is to examine the ^{207}Pb NMR spectra as a function of composition. The lead site in $MAPbI_3$ is surrounded by eight MA ions in the second coordination shell. Each of these MA ions can be replaced by a DMA ion. This leads to several different possible surroundings of the lead ion, which can be described as $[Pb(MA)_{8-n}(DMA)_n]$ (ignoring isomers). Each of these environments will have a different effect on the electronic environment of the Pb nucleus and will lead to a resonance at a different chemical shift in the ^{207}Pb spectrum. Using the observed signal integrals of the different resonances in the ^{207}Pb spectrum, the relative occurrence of each of these environments can be established. If these occurrences do not follow a binomial distribution, which can be calculated on the basis of the overall MA and DMA contents as determined using the ^{13}C spectra, then the distribution is not random and the clustering of ions or phase segregation must be occurring. This method has been applied successfully for perovskite systems containing mixtures of Cl and Br, showing that these ions are randomly distributed over the material.[65]

The ^{207}Pb spectra of the mixed MA/DMA systems are shown in Figure 3. This figure shows that ^{207}Pb NMR can clearly distinguish $MAPbI_3$ and $DMAPbI_3$, displaying resonances at either ~1400 or ~1000 ppm.[23] For the mixed MA/DMA cases, we observe a single broad line, which cannot be unambiguously deconvoluted into resonance lines of a series of well-defined environments. Clearly, the line width of the resonances is too large to observe the chemical shift differences among the different $[Pb(MA)_{8-n}(DMA)_n]$ sites. However, we

https://dx.doi.org/10.1021/acs.inorgchem.9b03380
Inorg. Chem. 2020, 59, 3730−3739

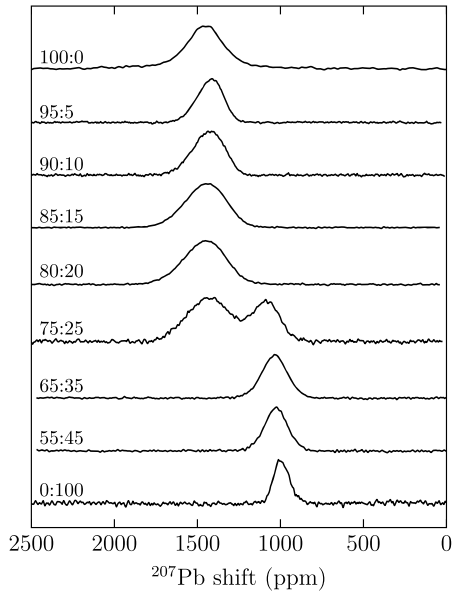

Figure 3. Static ^{207}Pb echo NMR spectra of $MA_{1-x}DMA_xPbI_3$ at 850 MHz. The values on the left are MA/DMA ratios of the solutions as used during synthesis.

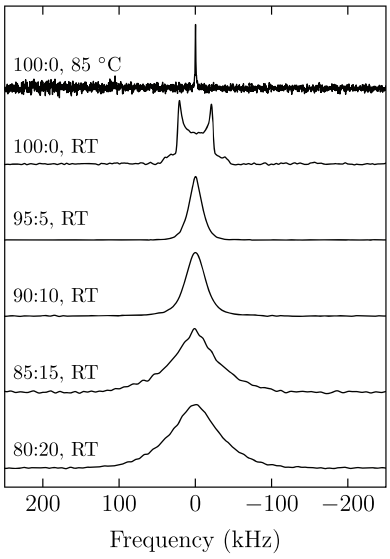

Figure 4. Static ^{14}N echo NMR spectra of $MA_{1-x}DMA_xPbI_3$ at 850 MHz using 30 kHz ^{1}H decoupling. The values on the left are MA/DMA ratios of the solutions as used during synthesis. Also shown is the spectrum for $MAPbI_3$ in the cubic phase (at 85 °C).

do observe changes upon DMA incorporation: the observed signal has more intensity at high ppm values (compare the 0:100 and 80:20 spectra). This indicates that the DMA-rich environments have a higher chemical shift than the MA-rich environments. Due to the severe overlap of these resonances, no conclusion can be drawn with respect to their relative occurrence, making it impossible to distinguish between clustering and solid solution behavior based on these data.

A similar conclusion can be drawn for the samples of $DMAPbI_3$ with MA incorporation (i.e., 75:25 and higher DMA content): the addition of MA leads to a broadening of the resonance toward higher ppm values, but no distinct sites can be identified.

As demonstrated above, ^{207}Pb NMR cannot, in this case, provide information on the distribution of the MA and DMA ions throughout the lattice. We therefore turn to ^{14}N NMR to obtain this information. The ^{14}N nucleus has a spin quantum number of 1, making it a quadrupolar nucleus. The NMR spectra of these nuclei are influenced by electric field gradients at the nuclear site. Due to this effect, ^{14}N spectra are very sensitive to the environment of the nitrogen nucleus. Each unique nitrogen site in a material will therefore lead to a different quadrupolar coupling and can be observed in a ^{14}N NMR spectrum as a well-defined powder pattern. Using ^{14}N NMR, we should therefore be able to identify whether there are several distinct environments or a whole distribution of local coordinations, giving some indication of the distribution of MA and DMA throughout the lattice.

Figure 4 shows the static ^{14}N spectra of the five $MA_{1-x}DMA_xPbI_3$ materials with $x < 0.21$. For the 100:0 case at room temperature, we observe a quadrupolar powder pattern typical of a site with an asymmetry parameter η of 0, which is expected for the symmetry of the MA site in the tetragonal phase.[57,66] The width of this powder pattern is much less than is to be expected for a stationary MA moiety because significant motional averaging takes place.[57] When raising the temperature, the pattern narrows, merging in a single narrow line at the tetragonal-phase to cubic-phase transition.[57] That the essentially asymmetric MA moiety can have such a high apparent symmetry is due to the fast reorientation of its C−N axis over a large number of isotropic orientations within the cavity, leading to overall time-averaged cubic symmetry.[31] This is shown in Figure 4 for the 100:0 sample at 85 °C. (For ^{14}N spectra of $MAPbI_3$ at intermediate temperatures, we refer to ref 67.)

For the samples with DMA incorporation (i.e., 95:5, 90:10, 85:15, and 80:20), we observe a single peak without any distinct features. The width of this resonance increases with increasing DMA content. Due to the lack of observable features, it is clear that we cannot describe this system using a single set of quadrupolar parameters (C_Q and η) or even two sets for MA and DMA. The observed continuous line shape can be explained only by assuming a wide range of different C_Q and η values, with no preferential values with a higher occurrence than the rest. This means that there must be a continuous variation in the local environment of the observed ^{14}N nuclei. These observations indicate that the MA and DMA ions must be distributed randomly throughout the lattice, with no observable clustering. The material is therefore a solid solution of MA and DMA within the inorganic Pb−I framework.

A remarkable effect that can be seen in Figure 4 is that the resonance observed for the 95:5 sample is narrower than that of the 100:0 sample at room temperature. The width of this resonance is an indication of the size of the (average) quadrupolar interaction of the ^{14}N spins, which is strongly influenced by the symmetry of the MA site in the lattice and the MA dynamics, as is described above. The reduced width of the ^{14}N resonance for the 95:5 sample compared to the line width of the 100:0 sample is therefore attributed to an increase in the symmetry of the sites occupied by the organic cations in the 95:5 sample compared to the symmetry of the cation cages in pure $MAPbI_3$ (100:0 sample). Apparently, the addition of DMA ions leads to an increase of the symmetry of the inorganic lattice. Possibly, the insertion of small amounts of the larger DMA ions relieves some strain in the material, allowing

https://dx.doi.org/10.1021/acs.inorgchem.9b03380
Inorg. Chem. 2020, 59, 3730−3739

the MA ions to move more freely. The exact background of this effect needs further investigation, however.

When more DMA is incorporated into the $MAPbI_3$ structure, the width of the ^{14}N resonance increases, suggesting that the effective symmetry of the cation sites is lowered upon further addition of DMA. This may simply be due to the fact that increased amounts of DMA in the structure lead to a larger variation in the local environment of the cations because neigboring cation cages will be populated with either MA or DMA cations. Alternatively, incorporating larger amounts of DMA may lead to more strain in the material (up to the point that a stable structure can no longer be formed at $x > 0.2$). We note that ^{13}C NMR shows a small shift of the MA resonance upon DMA incorporation (see the ^{13}C spectra of the 100:0 and 95:5 samples in Figure 2), which we attribute to a change of the lattice structure. Baikie et al. showed an equivalent shift to a higher ppm value going from the tetragonal to the cubic phase of $MAPbI_3$.[58]

In order to study the symmetry of the $MA_{1-x}DMA_xPbI_3$ structures in more detail, we turn to powder X-ray diffraction. Figure 5 shows the low-angle region of the diffractograms of

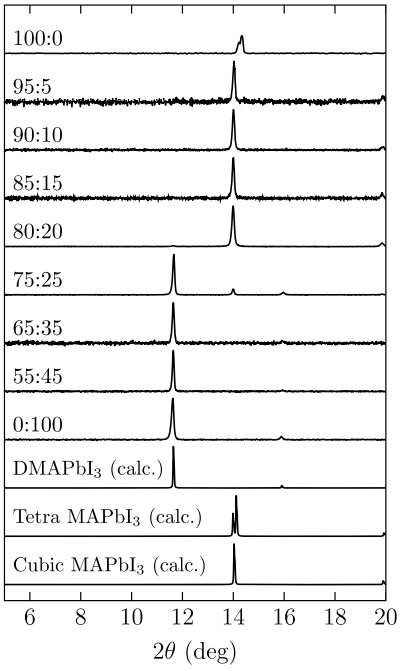

Figure 5. Powder XRD data of the $MA_{1-x}DMA_xPbI_3$ materials. The values on the left are MA/DMA ratios of the solutions used during synthesis.

both the $MAPbI_3$- and $DMAPbI_3$-based materials. From this, it is clear that there is a large change in the structure between 80:20 and 75:25, in line with the transition to a $DMAPbI_3$-based lattice, as was already derived from the ^{13}C and ^{207}Pb NMR data. The 75:25 sample shows diffraction peaks belonging to both phases. No changes are observed between 75:25 (yellow phase) and 0:100, indicating that the MA incorporation which takes place in the 75:25, 65:35, and 55:45 samples does not lead to an observable difference in the long-range lattice order. This demonstrates that the electronic structure remains largely unchanged when replacing a small number of DMA ions with (smaller) MA ions.

More interesting effects are observed when going from pure $MAPbI_3$ (i.e., the 100:0 sample) to a structure with DMA incorporated (i.e., 95:5, 90:10, 85:15, and 80:20). $MAPbI_3$ at room temperature is in a tetragonal phase, meaning that the crystallographic a and b axes are equal in length but the c axis is different.[31] This causes the diffraction peak at ∼14° to be split in two. As the a/b and the c axes are almost equal in length, these two lines are at nearly the same angle and partially overlap. When DMA is incorporated into the structure, these two lines merge and shift to a lower angle. This means that when DMA is incorporated into the lattice the a, b, and c axes become equal in length: the material adopts a cubic long-range order. This is in line with the ^{14}N NMR results discussed in the Solid-State NMR section: adding DMA to the $MAPbI_3$ structure increases the symmetry of the lattice. The shift to a lower angle is due to a slight increase in the unit cell dimensions, which also occurs for $MAPbI_3$ upon heating.[31] Between 95:5 and 80:20, no observable shift of the diffraction peak occurs, indicating that the unit cell dimensions do not change upon changing the amount of DMA in the cubic structure.

In a sense, the structure of the 95:5, 90:10, 85:15, and 80:20 samples can never be perfectly cubic: the positional disorder of the MA and DMA ions inhibits the description of the system using regular crystallographic means because there is no translation symmetry. Moreover, the ^{14}N NMR results state that the nitrogen environments have nonzero time-averaged quadrupolar coupling, opposing the claim of XRD concerning a cubic lattice. A way to understand these conflicting perceptions is to realize that XRD is mostly influenced by the long-range order in the Pb−I lattice (these contain the majority of the electrons that cause the diffraction). Clearly, the long-range order of the inorganic lattice points to a cubic structure, whereas the local environment of the organic moieties, as probed by NMR, does not indicate perfectly cubic local structure despite the fact that they rapidly reorientate in their cages. Despite the long-range order, we would still expect that the local disorder increases the line widths of the diffraction peaks as observed in the XRD experiments, but this is not clearly observed. However, without additional information on the source of the line widths (instrumental or otherwise), no conclusions can be drawn from the absence of such broadening of the diffraction peaks.

The cubic structure of the DMA-containing $MAPbI_3$-based materials at room temperature, as determined by XRD, suggests that the phase-transition temperature, which occurs at 55 °C for $MAPbI_3$, is lowered due to the addition of DMA. To study this in more detail, we performed a variable-temperature ^{14}N NMR study for the samples with r values of 100:0 to 80:20. We take the full width at half-maximum (fwhm) of the ^{14}N resonance as a rough measure of the average symmetry of the nitrogen environment (i.e., their cages in the lattice). Figure 6 shows the results obtained in this way. For the 100:0 material, the width of the pattern is very narrow above 55 °C (i.e., in the cubic phase). When lowering the temperature, the material transforms to a tetragonal phase, and the width of the ^{14}N NMR resonance increases as the unit cell asymmetry increases.[31,57,68,69] For the 95:5 sample, the line width is roughly constant between +45 and +10 °C. Below this, a clear increase in line width is observed, which levels off at −40 °C. For the 90:10 sample, a more dramatic increase in the line width upon cooling is observed, and the same is true for the 80:20 sample. All curves of the DMA-containing samples display a sigmoidal shape with a constant fwhm at high temperature and a distinct increase in line width with

https://dx.doi.org/10.1021/acs.inorgchem.9b03380
Inorg. Chem. 2020, 59, 3730−3739

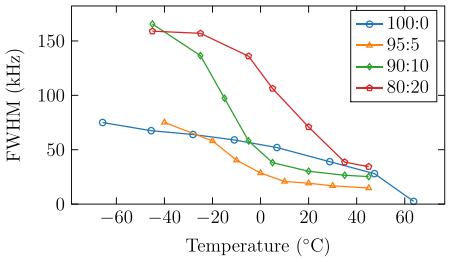

Figure 6. Full width at half-maximum (fwhm) of the static ^{14}N NMR spectra of several $MA_{1-x}DMA_xPbI_3$ powders as a function of temperature. For the spectra, see the Supporting Information.

decreasing T, indicative of a phase transition or a change in mobility. The constant fwhm at elevated temperature shows that the (averaged) local symmetry of the material no longer changes as a function of temperature and indicates that the materials can be considered to be cubic in this temperature range. The residual ^{14}N line width that is observed for the DMA-containing materials is caused by the positional disorder of the cations in the lattice: the random occupancy of the cavities in the structure by DMA or MA leads to a variation in the local environment resulting in a nonzero quadrupolar interaction for most of the MA and DMA ions. Upon cooling, the structure of the DMA-containing materials transforms to a lower symmetry, with the quadrupolar coupling steadily increasing until a new plateau is reached. When examining the curves for the 95:5 and 90:10 samples, it is clear that the increase in the fwhm starts at a lower temperature than for the 100:0 sample, showing that the 95:5 and 90:10 samples have a lower phase-transition temperature (∼10 °C) than the pure $MAPbI_3$ (100:0 sample). This suggests that the cubic phase in these materials is indeed stabilized due to the addition of the larger DMA cation. Qualitatively, this can be explained as follows: the addition of the larger DMA cation affects the cavities and therefore "pushes" the material to a higher-temperature structure. This is equivalent to increasing the Goldschmidt tolerance factor of the material.[70]

For the 80:20 material, the phase-transition temperature is higher than for the 95:5 and 90:10 samples. Possibly, the DMA content in this sample is so high that at lower temperatures, with lower cation reorientation dynamics, a high-symmetry structure is destabilized. This suggests that there is a minimum in the phase-transition temperature for a specific DMA content x between 0 and 0.207. Across the full range of temperatures sampled in Figure 6, the fwhm of the 80:20 sample is above that of the 100:0 sample. Nevertheless, XRD attributes a higher symmetry to the 80:20 sample, indicating that even at this high DMA content the inorganic sublattice is cubic at room temperature and above.

Reorientations of the organic cation play an important role in perovskite structures and are essential to the description of the observed symmetry of the different crystal phases. The reorientation process has been suggested to be important for the lifetime of charge carriers, electronic band structure, dielectric function, and absorption spectra of the material.[71−73] In $MAPbI_3$, the reorientation speed of the MA cation has been established at ∼3 ps.[74]

In order to quantify the reorientation speed of the MA and DMA cations in our structures, we acquired ^{14}N T_1 spin−lattice relaxation curves for both ions in the 80:20 sample under magic angle spinning conditions. This resulted in T_1 values of 121 ms for MA and 36 ms for DMA. (See the SI for the fits.) If we assume that the T_1 relaxation is dominated by quadrupolar relaxation, we can establish the correlation time of the reorientation motion based on the observed T_1 and the static quadrupolar coupling constant C_Q. Assuming reorientations in an isotropic potential, we can follow the method of Knop et al., who used $1/T_1 = 3/2\pi^2 C_Q^2 \tau_c$ to establish τ_c.[68] The static ^{14}N C_Q can be calculated using density functional theory (DFT), as we have done for $MAPbI_3$ in our previous work.[57] Performing these calculations for the cell dimensions of the samples studied in this work, we obtain static C_Q values of 670 kHz for MA and 596 kHz for DMA. Using the equation above, this leads to τ_c = 1.24 ps for MA and 2.62 ps for DMA. Although the DMA ion reorients more slowly than the MA ion in this structure, it is clear that it is still very mobile, and both values are of the same order of magnitude as was established for the MA cation in $MAPbI_3$.

For the application of $MA_{1-x}DMA_xPbI_3$ in PV devices, the optical properties of the material are essential. For other mixed cation systems, the band gap shows changes with respect to $MAPbI_3$.[75,76] To verify whether there are any changes in the optical properties upon DMA incorporation, reflection data for powders of up to 80:20 were obtained. The results of these measurements are shown in Figure 7. For the 100:0, 95:5, and

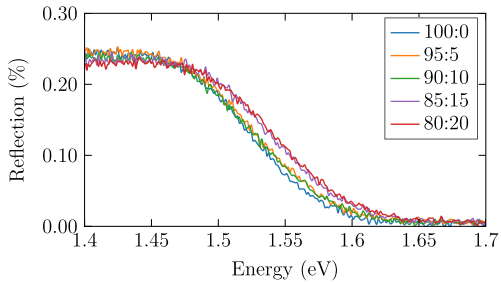

Figure 7. Reflection data for $MA_{1-x}DMA_xPbI_3$ powder. Only data for the "black" materials are plotted ($x \leq 0.207$).

90:10 powders, a similar curve is observed. However, for the 85:15 and 80:20 samples a small shift to higher energy occurs. The size of this shift is about +20 meV and is of the same order of magnitude as has been described for $MA_{1-x}DMA_xPbBr_3$.[24] Note that the band gap of $MAPbI_3$ is already a bit too high for the optimum efficiency of a single junction solar cell.[77−79] The addition of DMA to the $MAPbI_3$ structure is therefore detrimental to the PV efficiency if only band gap arguments are considered. However, given the small size of the shift, this is not significant.

CONCLUSIONS

We have synthesized $MA_{1-x}DMA_xPbI_3$ with $0 \leq x \leq 1$. Adding a small amount of DMA to $MAPbI_3$ (up to x = 0.20) lowers the phase-transition temperature from 55 to ∼10 °C and stabilizes the cubic phase at room temperature. The material has a 3D perovskite structure, with the MA and DMA ions distributed randomly over the cavities (the A sites) in the lattice. For $x > 0.72$, a nonperovskite phase is formed, which is essentially $DMAPbI_3$ with MA cations incorporated at the A site. For all levels of DMA in the precursors' solution, the resulting crystallized solid-state material was richer in DMA than the solution. This suggest that the formation energy of these mixed-ion materials is lower than that for pure $MAPbI_3$ or $DMAPbI_3$, which might be favorable to the thermodynamic

https://dx.doi.org/10.1021/acs.inorgchem.9b03380
Inorg. Chem. 2020, 59, 3730−3739

stability of the materials. The high levels of incorporation of DMA or MA ions in $MAPbI_3$ or $DMAPbI_3$ demonstrates the flexibility of these materials when it comes to the incorporation of other organic cations.

Materials with intermediate mixtures of MA and DMA ($0.20 < x < 0.72$) cannot be produced, as neither the $MAPbI_3$ nor the $DMAPbI_3$ structure can accommodate these high levels of DMA and MA. Using ^{14}N NMR relaxation experiments, the reorientation time of the MA and DMA cations in $MA_{0.8}DMA_{0.2}PbI_3$ was established at 1.6 and 2.6 ps, respectively, which is slightly faster than in pure $MAPbI_3$. The band gap of the perovskite phase is slightly increased by DMA incorporation, with a change of about +20 meV for the $x = 0.20$ sample.

■ ASSOCIATED CONTENT

Supporting Information

The Supporting Information is available free of charge at https://pubs.acs.org/doi/10.1021/acs.inorgchem.9b03380.

Drawings of the crystal structures of $MAPbI_3$ and $DMAPbI_3$; ^1H, ^{13}C, ^{207}Pb, and ^{14}N saturation recovery measurements of $MAPbI_3$, $DMAPbI_3$, and DMA in $MAPbI_3$; and variable-temperature ^{14}N spectra used to generate Figure 6 (PDF)

■ AUTHOR INFORMATION

Corresponding Author

Arno P. M. Kentgens − *Magnetic Resonance Research Center, Institute for Molecules and Materials, Radboud University 6525 AJ Nijmegen, The Netherlands;* orcid.org/0000-0001-5893-4488; Email: A.Kentgens@nmr.ru.nl

Authors

Wouter M. J. Franssen − *Magnetic Resonance Research Center, Institute for Molecules and Materials, Radboud University 6525 AJ Nijmegen, The Netherlands*

Cathy M. M. van Heumen − *Magnetic Resonance Research Center, Institute for Molecules and Materials, Radboud University 6525 AJ Nijmegen, The Netherlands*

Complete contact information is available at: https://pubs.acs.org/10.1021/acs.inorgchem.9b03380

Notes

The authors declare no competing financial interest.

■ ACKNOWLEDGMENTS

The Netherlands Organization for Scientific Research (NWO) is acknowledged for its financial support of the program of the Graduate School for Molecules and Materials (W.M.J.F.). Moreover, NWO supports the solid-state NMR facility for advanced materials research which is part of the ultrahigh field NMR facilities for The Netherlands (uNMR-NL). Paul Tinnemans is acknowledged for the XRD experiments, and Gerard Bauhuis is acknowledged for assistance with the reflectance measurements. Gilles de Wijs is acknowledged for performing the DFT calculations.

■ REFERENCES

(1) Kojima, A.; Teshima, K.; Shirai, Y.; Miyasaka, T. Organometal halide perovskites as visible-light sensitizers for photovoltaic cells. *J. Am. Chem. Soc.* **2009**, *131*, 6050−6051.

(2) Cui, J.; Yuan, H.; Li, J.; Xu, X.; Shen, Y.; Lin, H.; Wang, M. Recent Progress in Efficient Hybrid Lead Halide Perovskite Solar Cells. *Sci. Technol. Adv. Mater.* **2015**, *16*, 036004.

(3) NREL efficiency chart. https://www.nrel.gov/pv/assets/pdfs/best-research-cell-efficiencies.20191106.pdf.

(4) Hailegnaw, B.; Kirmayer, S.; Edri, E.; Hodes, G.; Cahen, D. Rain on methylammonium lead iodide based perovskites: possible environmental effects of perovskite solar cells. *J. Phys. Chem. Lett.* **2015**, *6*, 1543−1547.

(5) Niu, G.; Guo, X.; Wang, L. Review of recent progress in chemical stability of perovskite solar cells. *J. Mater. Chem. A* **2015**, *3*, 8970−8980.

(6) Weerasinghe, H. C.; Dkhissi, Y.; Scully, A. D.; Caruso, R. A.; Cheng, Y.-B. Encapsulation for improving the lifetime of flexible perovskite solar cells. *Nano Energy* **2015**, *18*, 118−125.

(7) Wong-Stringer, M.; Game, O. S.; Smith, J. A.; Routledge, T. J.; Alqurashy, B. A.; Freestone, B. G.; Parnell, A. J.; Vaenas, N.; Kumar, V.; Alawad, M. O. A.; Iraqi, A.; Rodenburg, C.; Lidzey, D. G. High-Performance Multilayer Encapsulation for Perovskite Photovoltaics. *Adv. Energy Mater.* **2018**, *8*, 1801234.

(8) De Marco, N.; Zhou, H.; Chen, Q.; Sun, P.; Liu, Z.; Meng, L.; Yao, E.-P.; Liu, Y.; Schiffer, A.; Yang, Y. Guanidinium: a route to enhanced carrier lifetime and open-circuit voltage in hybrid perovskite solar cells. *Nano Lett.* **2016**, *16*, 1009−1016.

(9) Kubicki, D. J.; Prochowicz, D.; Hofstetter, A.; Saski, M.; Yadav, P.; Bi, D.; Pellet, N.; Lewiński, J.; Zakeeruddin, S. M.; Grätzel, M.; Emsley, L. Formation of Stable Mixed Guanidinium−Methylammonium Phases with Exceptionally Long Carrier Lifetimes for High-Efficiency Lead Iodide-Based Perovskite Photovoltaics. *J. Am. Chem. Soc.* **2018**, *140*, 3345−3351.

(10) Yang, W. S.; Park, B.-W.; Jung, E. H.; Jeon, N. J.; Kim, Y. C.; Lee, D. U.; Shin, S. S.; Seo, J.; Kim, E. K.; Noh, J. H.; Seok, S. I. Iodide management in formamidinium-lead-halide−based perovskite layers for efficient solar cells. *Science* **2017**, *356*, 1376−1379.

(11) Li, Z.; Yang, M.; Park, J.-S.; Wei, S.-H.; Berry, J. J.; Zhu, K. Stabilizing perovskite structures by tuning tolerance factor: formation of formamidinium and cesium lead iodide solid-state alloys. *Chem. Mater.* **2016**, *28*, 284−292.

(12) Choi, H.; Jeong, J.; Kim, H.-B.; Kim, S.; Walker, B.; Kim, G.-H.; Kim, J. Y. Cesium-doped methylammonium lead iodide perovskite light absorber for hybrid solar cells. *Nano Energy* **2014**, *7*, 80−85.

(13) Saliba, M.; Matsui, T.; Seo, J.-Y.; Domanski, K.; Correa-Baena, J.-P.; Nazeeruddin, M. K.; Zakeeruddin, S. M.; Tress, W.; Abate, A.; Hagfeldt, A.; Grätzel, M. Cesium-containing triple cation perovskite solar cells: improved stability, reproducibility and high efficiency. *Energy Environ. Sci.* **2016**, *9*, 1989−1997.

(14) Eperon, G. E.; Stranks, S. D.; Menelaou, C.; Johnston, M. B.; Herz, L. M.; Snaith, H. J. Formamidinium lead trihalide: a broadly tunable perovskite for efficient planar heterojunction solar cells. *Energy Environ. Sci.* **2014**, *7*, 982−988.

(15) McMeekin, D. P.; Sadoughi, G.; Rehman, W.; Eperon, G. E.; Saliba, M.; Hörantner, M. T.; Haghighirad, A.; Sakai, N.; Korte, L.; Rech, B.; Johnston, M. B.; Herz, L. M.; Snaith, H. J. A mixed-cation lead mixed-halide perovskite absorber for tandem solar cells. *Science* **2016**, *351*, 151−155.

(16) Volonakis, G.; Filip, M. R.; Haghighirad, A. A.; Sakai, N.; Wenger, B.; Snaith, H. J.; Giustino, F. Lead-free halide double perovskites via heterovalent substitution of noble metals. *J. Phys. Chem. Lett.* **2016**, *7*, 1254−1259.

(17) Giustino, F.; Snaith, H. J. Toward Lead-Free Perovskite Solar Cells. *ACS Energy Lett.* **2016**, *1*, 1233−1240.

(18) Nie, W.; Tsai, H.; Asadpour, R.; Blancon, J.-C.; Neukirch, A. J.; Gupta, G.; Crochet, J. J.; Chhowalla, M.; Tretiak, S.; Alam, M. A.; Wang, H.-L.; Mohite, A. D. High-efficiency solution-processed perovskite solar cells with millimeter-scale grains. *Science* **2015**, *347*, 522−525.

(19) Jana, A.; Mittal, M.; Singla, A.; Sapra, S. Solvent-free, mechanochemical syntheses of bulk trihalide perovskites and their nanoparticles. *Chem. Commun.* **2017**, *53*, 3046−3049.

(20) Poglitsch, A.; Weber, D. Dynamic disorder in methylammoniumtrihalogenoplumbates (II) observed by millimeter-wave spectroscopy. *J. Chem. Phys.* **1987**, *87*, 6373−6378.
(21) Prochowicz, D.; Saski, M.; Yadav, P.; Grätzel, M.; Lewiński, J. Mechanoperovskites for Photovoltaic Applications: Preparation, Characterization, and Device Fabrication. *Acc. Chem. Res.* **2019**, *52*, 3233−3243.
(22) Jodlowski, A. D.; Yépez, A.; Luque, R.; Camacho, L.; de Miguel, G. Benign-by-Design Solventless Mechanochemical Synthesis of Three-, Two-, and One-Dimensional Hybrid Perovskites. *Angew. Chem., Int. Ed.* **2016**, *55*, 14972−14977.
(23) Franssen, W. M. J.; Bruijnaers, B. J.; Portengen, V. H. L.; Kentgens, A. P. M. Dimethylammonium Incorporation in Lead Acetate Based $MAPbI_3$ Perovskite Solar Cells. *ChemPhysChem* **2018**, *19*, 3107−3115.
(24) Anelli, C.; Chierotti, M. R.; Bordignon, S.; Quadrelli, P.; Marongiu, D.; Bongiovanni, G.; Malavasi, L. Investigation of Dimethylammonium Solubility in $MAPbBr_3$ Hybrid Perovskite: Synthesis, Crystal Structure, and Optical Properties. *Inorg. Chem.* **2019**, *58*, 944−949.
(25) Ke, W.; Spanopoulos, I.; Stoumpos, C. C.; Kanatzidis, M. G. Myths and reality of $HPbI_3$ in halide perovskite solar cells. *Nat. Commun.* **2018**, *9*, 4785.
(26) Wang, Y.; Liu, X.; Zhang, T.; Wang, X.; Kan, M.; Shi, J.; Zhao, Y. The Role of Dimethylammonium Iodide in $CsPbI_3$ Perovskite Fabrication: Additive or Dopant? *Angew. Chem., Int. Ed.* **2019**, *58*, 16691−16696.
(27) Ju, D.; Zhao, T.; Yangyang, D.; Zhang, G.; Hu, X.; Cui, D.; Tao, X. Gas induced conversion of hybrid perovskite single crystal to single crystal for great enhancement of their photoelectric properties. *J. Mater. Chem. A* **2017**, *5*, 21919−21925.
(28) García-Fernández, A.; Bermúdez-García, J. M.; Castro-García, S.; Llamas-Saiz, A. L.; Artiaga, R.; López-Beceiro, J.; Hu, S.; Ren, W.; Stroppa, A.; Sánchez-Andújar, M.; Señarís Rodríguez, M. A. Phase Transition, Dielectric Properties, and Ionic Transport in the [(CH3) 2NH2] PbI3 Organic−Inorganic Hybrid with 2H-Hexagonal Perovskite Structure. *Inorg. Chem.* **2017**, *56*, 4918−4927.
(29) García-Fernández, A.; Bermúdez-García, J. M.; Castro-García, S.; Llamas-Saiz, A. L.; Artiaga, R.; López-Beceiro, J. J.; Sánchez-Andújar, M.; Señarís Rodríguez, M. A. [(CH3)2NH2]7Pb4 × 15 (X = Cl and Br), 2D-Perovskite Related Hybrids with Dielectric Transitions and Broadband Photoluminiscent Emission. *Inorg. Chem.* **2018**, *57*, 3215−3222.
(30) Kieslich, G.; Sun, S.; Cheetham, A. K. Solid-state principles applied to organic−inorganic perovskites: new tricks for an old dog. *Chem. Sci.* **2014**, *5*, 4712−4715.
(31) Weller, M. T.; Weber, O. J.; Henry, P. F.; Di Pumpo, A. M.; Hansen, T. C. Complete structure and cation orientation in the perovskite photovoltaic methylammonium lead iodide between 100 and 352 K. *Chem. Commun.* **2015**, *51*, 4180−4183.
(32) Yi, C.; Luo, J.; Meloni, S.; Boziki, A.; Ashari-Astani, N.; Grätzel, C.; Zakeeruddin, S. M.; Röthlisberger, U.; Grätzel, M. Entropic stabilization of mixed A-cation ABX_3 metal halide perovskites for high performance perovskite solar cells. *Energy Environ. Sci.* **2016**, *9*, 656−662.
(33) Han, Q.; Bae, S.-H.; Sun, P.; Hsieh, Y.-T.; Yang, Y. M.; Rim, Y. S.; Zhao, H.; Chen, Q.; Shi, W.; Li, G.; Yang, Y. Single Crystal Formamidinium Lead Iodide (FAPbI3): Insight into the Structural, Optical, and Electrical Properties. *Adv. Mater.* **2016**, *28*, 2253−2258.
(34) Yang, W. S.; Park, B.-W.; Jung, E. H.; Jeon, N. J.; Kim, Y. C.; Lee, D. U.; Shin, S. S.; Seo, J.; Kim, E. K.; Noh, J. H.; Seok, S. I. Iodide management in formamidinium-lead-halide−based perovskite layers for efficient solar cells. *Science* **2017**, *356*, 1376−1379.
(35) Pellet, N.; Gao, P.; Gregori, G.; Yang, T.-Y.; Nazeeruddin, M. K.; Maier, J.; Grätzel, M. Mixed-organic-cation Perovskite photovoltaics for enhanced solar-light harvesting. *Angew. Chem., Int. Ed.* **2014**, *53*, 3151−3157.
(36) Prochowicz, D.; Yadav, P.; Saliba, M.; Saski, M.; Zakeeruddin, S. M.; Lewiński, J.; Grätzel, M. Mechanosynthesis of pure phase mixed-cation MA x FA 1- x PbI 3 hybrid perovskites: photovoltaic performance and electrochemical properties. *Sustainable Energy Fuels* **2017**, *1*, 689−693.
(37) Saliba, M.; Matsui, T.; Seo, J.-Y.; Domanski, K.; Correa-Baena, J.-P.; Nazeeruddin, M. K.; Zakeeruddin, S. M.; Tress, W.; Abate, A.; Hagfeldt, A.; Grätzel, M. Cesium-containing triple cation perovskite solar cells: improved stability, reproducibility and high efficiency. *Energy Environ. Sci.* **2016**, *9*, 1989−1997.
(38) Saidaminov, M. I.; Abdelhady, A. L.; Murali, B.; Alarousu, E.; Burlakov, V. M.; Peng, W.; Dursun, I.; Wang, L.; He, Y.; Maculan, G.; Goriely, A.; Wu, T.; Mohammed, O. F.; Bakr, O. M. High-quality bulk hybrid perovskite single crystals within minutes by inverse temperature crystallization. *Nat. Commun.* **2015**, *6*, 7586.
(39) van Meerten, S. G. J.; Franssen, W. M. J.; Kentgens, A. P. M. ssNake: A cross-platform open-source NMR data processing and fitting application. *J. Magn. Reson.* **2019**, *301*, 56−66.
(40) Tong, Y. Y. Nuclear spin-echo Fourier-transform mapping spectroscopy for broad NMR lines in solids. *J. Magn. Reson., Ser. A* **1996**, *119*, 22−28.
(41) Momma, K.; Izumi, F. VESTA 3 for three-dimensional visualization of crystal, volumetric and morphology data. *J. Appl. Crystallogr.* **2011**, *44*, 1272−1276.
(42) Mancini, A.; Quadrelli, P.; Amoroso, G.; Milanese, C.; Boiocchi, M.; Sironi, A.; Patrini, M.; Guizzetti, G.; Malavasi, L. Synthesis, structural and optical characterization of APbX3 (A= methylammonium, dimethylammonium, trimethylammonium; X= I, Br, Cl) hybrid organic-inorganic materials. *J. Solid State Chem.* **2016**, *240*, 55−60.
(43) Whitfield, P. S.; Herron, N.; Guise, W. E.; Page, K.; Cheng, Y. Q.; Milas, I.; Crawford, M. K. Structures, phase transitions and tricritical behavior of the hybrid perovskite methyl ammonium lead iodide. *Sci. Rep.* **2016**, *6*, 35685.
(44) Szafrański, M.; Katrusiak, A. Mechanism of pressure-induced phase transitions, amorphization, and absorption-edge shift in photovoltaic methylammonium lead iodide. *J. Phys. Chem. Lett.* **2016**, *7*, 3458−3466.
(45) Petrilli, H. M.; Blöchl, P. E.; Blaha, P.; Schwarz, K. Electric-Field-Gradient Calculations Using the Projector Augmented Wave Method. *Phys. Rev. B: Condens. Matter Mater. Phys.* **1998**, *57*, 14690−14697.
(46) Kresse, G.; Hafner, J. Ab Initio Molecular Dynamics for Liquid Metals. *Phys. Rev. B: Condens. Matter Mater. Phys.* **1993**, *47*, 558−561.
(47) Kresse, G.; Hafner, J. Ab Initio Molecular-Dynamics Simulation of the Liquid-Metal−Amorphous-Semiconductor Transition in Germanium. *Phys. Rev. B: Condens. Matter Mater. Phys.* **1994**, *49*, 14251−14269.
(48) Kresse, G.; Furthmüller, J. Efficiency of Ab-Initio Total Energy Calculations for Metals and Semiconductors Using a Plane-Wave Basis Set. *Comput. Mater. Sci.* **1996**, *6*, 15−50.
(49) Kresse, G.; Furthmüller, J. Efficient Iterative Schemes for Ab Initio Total-Energy Calculations Using a Plane-Wave Basis Set. *Phys. Rev. B: Condens. Matter Mater. Phys.* **1996**, *54*, 11169−11186.
(50) Blöchl, P. E. Projector Augmented-Wave Method. *Phys. Rev. B: Condens. Matter Mater. Phys.* **1994**, *50*, 17953−17979.
(51) Kresse, G. From Ultrasoft Pseudopotentials to the Projector Augmented-Wave Method. *Phys. Rev. B: Condens. Matter Mater. Phys.* **1999**, *59*, 1758−1775.
(52) Perdew, J. P.; Burke, K.; Ernzerhof, M. Generalized Gradient Approximation Made Simple. *Phys. Rev. Lett.* **1996**, *77*, 3865−3868.
(53) Monkhorst, H. J.; Pack, J. D. Special points for Brillouin-zone integrations. *Phys. Rev. B* **1976**, *13*, 5188−5192.
(54) King-Smith, R. D.; Payne, M. C.; Lin, J. S. Real-space implementation of nonlocal pseudopotentials for first-principles total-energy calculations. *Phys. Rev. B: Condens. Matter Mater. Phys.* **1991**, *44*, 13063−13066.
(55) Kresse, G.; Marsman, M.; Furthmüller, J. *VASP the Guide*; 2015, https://www.vasp.at/wiki/index.php/The_VASP_Manual.
(56) Pyykkö, P. Year-2008 nuclear quadrupole moments. *Mol. Phys.* **2008**, *106*, 1965−1974.

https://dx.doi.org/10.1021/acs.inorgchem.9b03380
Inorg. Chem. 2020, 59, 3730−3739

(57) Franssen, W. M. J.; van Es, S. G. D.; Dervişoğlu, R.; de Wijs, G. A.; Kentgens, A. P. M. Symmetry, Dynamics, and Defects in Methylammonium Lead Halide Perovskites. *J. Phys. Chem. Lett.* **2017**, *8*, 61−66.
(58) Baikie, T.; Barrow, N. S.; Fang, Y.; Keenan, P. J.; Slater, P. R.; Piltz, R. O.; Gutmann, M.; Mhaisalkar, S. G.; White, T. J. A combined single crystal neutron/X-ray diffraction and solid-state nuclear magnetic resonance study of the hybrid perovskites $CH_3NH_3PbX_3$ (X = I, Br and Cl). *J. Mater. Chem. A* **2015**, *3*, 9298−9307.
(59) Rosales, B. A.; Men, L.; Cady, S. D.; Hanrahan, M. P.; Rossini, A. J.; Vela, J. Persistent dopants and phase segregation in organolead mixed-halide perovskites. *Chem. Mater.* **2016**, *28*, 6848−6859.
(60) Pareja-Rivera, C.; Solís-Cambero, A. L.; Sánchez-Torres, M.; Lima, E.; Solis-Ibarra, D. On the True Composition of Mixed-Cation Perovskite Films. *ACS Energy Lett.* **2018**, *3*, 2366−2367.
(61) Brunetti, B.; Cavallo, C.; Ciccioli, A.; Gigli, G.; Latini, A. On the thermal and thermodynamic (in) stability of methylammonium lead halide perovskites. *Sci. Rep.* **2016**, *6*, 31896.
(62) Askar, A. M.; Bernard, G. M.; Wiltshire, B.; Shankar, K.; Michaelis, V. K. Multinuclear Magnetic Resonance Tracking of Hydro, Thermal, and Hydrothermal Decomposition of $CH_3NH_3PbI_3$. *J. Phys. Chem. C* **2017**, *121*, 1013−1024.
(63) Nagabhushana, G.; Shivaramaiah, R.; Navrotsky, A. Direct calorimetric verification of thermodynamic instability of lead halide hybrid perovskites. *Proc. Natl. Acad. Sci. U. S. A.* **2016**, *113*, 7717−7721.
(64) Li, W.-G.; Rao, H.-S.; Chen, B.-X.; Wang, X.-D.; Kuang, D.-B. A formamidinium−methylammonium lead iodide perovskite single crystal exhibiting exceptional optoelectronic properties and long-term stability. *J. Mater. Chem. A* **2017**, *5*, 19431−19438.
(65) Karmakar, A.; Askar, A. M.; Bernard, G. M.; Terskikh, V. V.; Ha, M.; Patel, S.; Shankar, K.; Michaelis, V. K. Mechanochemical Synthesis of Methylammonium Lead Mixed−Halide Perovskites: Unraveling the Solid-Solution Behavior using Solid-State NMR. *Chem. Mater.* **2018**, *30*, 2309−2321.
(66) Kubicki, D. J.; Prochowicz, D.; Hofstetter, A.; Péchy, P.; Zakeeruddin, S. M.; Grätzel, M.; Emsley, L. Cation Dynamics in Mixed-Cation $(MA)_x(FA)_{1-x}PbI_3$ Hybrid Perovskites from Solid-State NMR. *J. Am. Chem. Soc.* **2017**, *139*, 10055−10061.
(67) Bernard, G. M.; Wasylishen, R. E.; Ratcliffe, C. I.; Terskikh, V.; Wu, Q.; Buriak, J. M.; Hauger, T. Methylammonium Cation Dynamics in Methylammonium Lead Halide Perovskites: A Solid-State NMR Perspective. *J. Phys. Chem. A* **2018**, *122*, 1560−1573.
(68) Knop, O.; Wasylishen, R. E.; White, M. A.; Cameron, T. S.; Oort, M. J. M. V. Alkylammonium lead halides. Part 2. $CH_3NH_3PbX_3$ (X = Cl, Br, I) perovskites: cuboctahedral halide cages with isotropic cation reorientation. *Can. J. Chem.* **1990**, *68*, 412−422.
(69) G, S.; Mahale, P.; Kore, B. P.; Mukherjee, S.; Pavan, M. S.; De, C.; Ghara, S.; Sundaresan, A.; Pandey, A.; Guru Row, T. N.; Sarma, D. D. Is $CH_3NH_3PbI_3$ Polar? *J. Phys. Chem. Lett.* **2016**, *7*, 2412−2419.
(70) Goldschmidt, V. M. Die gesetze der krystallochemie. *Naturwissenschaften* **1926**, *14*, 477−485.
(71) Gong, J.; Yang, M.; Ma, X.; Schaller, R. D.; Liu, G.; Kong, L.; Yang, Y.; Beard, M. C.; Lesslie, M.; Dai, Y.; Huang, B.; Zhu, K.; Xu, T. Electron−Rotor Interaction in Organic−Inorganic Lead Iodide Perovskites Discovered by Isotope Effects. *J. Phys. Chem. Lett.* **2016**, *7*, 2879−2887.
(72) Motta, C.; El-Mellouhi, F.; Kais, S.; Tabet, N.; Alharbi, F.; Sanvito, S. Revealing the role of organic cations in hybrid halide perovskite $CH_3NH_3PbI_3$. *Nat. Commun.* **2015**, *6*, 7026.
(73) Mehdizadeh, A.; Akhtarianfar, S. F.; Shojaei, S. Role of Methylammonium Rotation in Hybrid Halide $MAPbX_3$ (X = I, Br, and Cl) Perovskites by a Density Functional Theory Approach: Optical and Electronic Properties. *J. Phys. Chem. C* **2019**, *123*, 6725−6734.
(74) Bakulin, A. A.; Selig, O.; Bakker, H. J.; Rezus, Y. L.; Müller, C.; Glaser, T.; Lovrincic, R.; Sun, Z.; Chen, Z.; Walsh, A.; Frost, J. M.; Jansen, T. L. C. Real-Time Observation of Organic Cation Reorientation in Methylammonium Lead Iodide Perovskites. *J. Phys. Chem. Lett.* **2015**, *6*, 3663−3669.
(75) Amat, A.; Mosconi, E.; Ronca, E.; Quarti, C.; Umari, P.; Nazeeruddin, M. K.; Grätzel, M.; De Angelis, F. Cation-induced band-gap tuning in organohalide perovskites: interplay of spin−orbit coupling and octahedra tilting. *Nano Lett.* **2014**, *14*, 3608−3616.
(76) Borriello, I.; Cantele, G.; Ninno, D. Ab initio investigation of hybrid organic-inorganic perovskites based on tin halides. *Phys. Rev. B: Condens. Matter Mater. Phys.* **2008**, *77*, 235214.
(77) Jiang, S.; Fang, Y.; Li, R.; Xiao, H.; Crowley, J.; Wang, C.; White, T. J.; Goddard, W. A., III; Wang, Z.; Baikie, T.; Fang, J. Pressure-Dependent Polymorphism and Band-Gap Tuning of Methylammonium Lead Iodide Perovskite. *Angew. Chem., Int. Ed.* **2016**, *55*, 6540−6544.
(78) Quarti, C.; Mosconi, E.; Ball, J. M.; D'Innocenzo, V.; Tao, C.; Pathak, S.; Snaith, H. J.; Petrozza, A.; De Angelis, F. Structural and optical properties of methylammonium lead iodide across the tetragonal to cubic phase transition: implications for perovskite solar cells. *Energy Environ. Sci.* **2016**, *9*, 155−163.
(79) Rühle, S. Tabulated values of the Shockley−Queisser limit for single junction solar cells. *Sol. Energy* **2016**, *130*, 139−147.

https://dx.doi.org/10.1021/acs.inorgchem.9b03380
Inorg. Chem. 2020, 59, 3730−3739